Localized States and Resultant Band Bending in Graphene Antidot Superlattices

Milan Begliarbekov,[†] Onejae Sul,[‡] John Santanello,[†] Nan Ai,[†] Xi Zhang,[†] Eui-Hyeok Yang,[‡] and Stefan Strauf[*,†]

[†]Department of Physics and Engineering Physics and [‡]Department of Mechanical Engineering, Stevens Institute of Technology, Hoboken, New Jersey 07030, United States

S *Supporting Information*

ABSTRACT: We fabricated dye sensitized graphene antidot superlattices with the purpose of elucidating the role of the localized edge state density. The fluorescence from deposited dye molecules was found to strongly quench as a function of increasing antidot filling fraction, whereas it was enhanced in unpatterned but electrically backgated samples. This contrasting behavior is strongly indicative of a built-in lateral electric field that accounts for fluorescence quenching as well as p-type doping. These findings are of great interest for light-harvesting applications that require field separation of electron−hole pairs.

KEYWORDS: Antidot, graphene superlattice, band bending
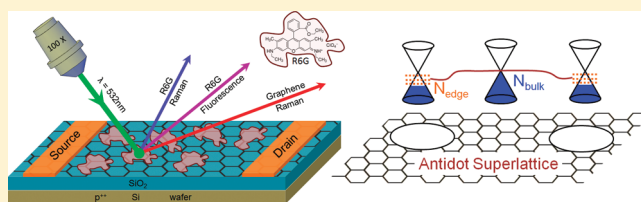
Graphene, a two-dimensional monolayer of carbon atoms arranged in a hexagonal lattice, has been recently isolated[1] and shown to exhibit excellent electrical,[2,3] thermal,[4] mechanical,[5] and optical[6] properties. Electron transport has been studied extensively in single- and few-layer graphene sheets,[7,8] while optoelectronic properties and light−matter interaction in nanostructured graphene gain increasingly more interest in the research community, in particular since the advent of first ultrafast graphene photodetectors.[9] Single layer graphene absorbs only 2.3% of the incident radiation in the visible spectrum;[10] consequently, efficient photocarrier separation within graphene becomes particularly important. In order to create a built-in electrical field that facilitates carrier separation, silicon based technology relies on the pn-junction that is created by doping the silicon lattice. Physical doping of graphene has been previously achieved by addition of extrinsic atomic[11,12] or molecular[13,14] species either by adsorption or intercalation into the graphene lattice.[12,15] A potentially simpler way to make graphene a viable material for optoelectronics can be achieved by utilizing lateral electric fields created by Schottky barriers near the source and drain metal contacts,[9,16,17] as was previously done in carbon nanotubes.[18] In the presence of such metal contacts it was also observed that nanotube fluorescence can be significantly enhanced.[19] While graphene does not display any exciton emission, quantum dots placed on unpatterned graphene were recently shown to undergo strong fluorescence quenching, which is indicative of energy transfer from the quantum dot exciton oscillator into graphene.[20] Such hybrids between graphene and light harvesting molecules can potentially overcome the low absorption efficiency of bare graphene.

Nanostructured graphene offers further possibilities to explore light harvesting and carrier separation. Of particular interest are the so-called antidot superlattices, i.e., lattices comprised of a periodic arrangement of perforations in the underlying graphene structure. These superlattices were predicted to possess a non-negligible magnetic moment,[21] a small band gap[22−25] that can be controlled by the antidot filling fraction,[26,27] and Peierls type electron−hole coupling that leads to polaronic behavior.[26] In a previous work, Heydrich et al., showed that the introduction of an antidot superlattice results in the stiffening of the G band in graphene's Raman spectrum, as well as an energetic shift of the G and G′ bands commensurate with p-type doping.[28] Furthermore, recent theoretical predictions show that the periphery of graphene possesses a nonnegligible density of states N_{edge} that is spatially localized at the edges and is distinct from the bulk states N_{bulk} that are present in graphene's interior regions. Consequently, antidot superlattices provide a natural framework for studying these states and their properties, since the edge states in these systems coexist with the bulk states, unlike in dot lattices, where the ratio of edge to bulk states is small.
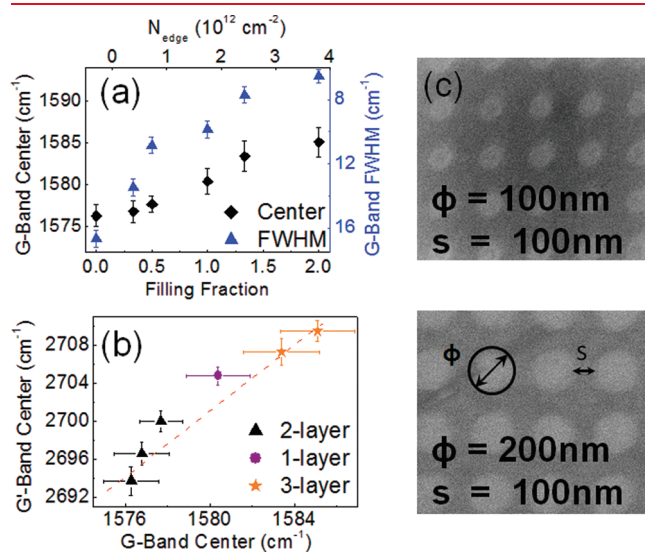
Here we report an electro-optical study of dye sensitized graphene antidot superlattices with the purpose of elucidating the role of the localized edge state density on its light-harvesting properties. The amount of p-type doping introduced by the edge states is quantified for various antidot filling fractions using confocal μ-Raman spectroscopy and transport measurements. We show that the fluorescence from deposited dye molecules strongly quenches in linear proportion to the antidot filling fraction, whereas it was enhanced in the presence of free carriers in unpatterned but electrically backgated samples. This contrasting behavior is strongly indicative of a built-in lateral electric field that accounts for fluorescence quenching as well as p-type doping

and the observed Raman signatures. Our study provides new insights into the interplay of localized edge states in antidot lattices and the resulting band bending, which are critical properties to enable novel applications of nanostructured graphene for light harvesting and photovoltaic devices.

Results and Discussion. *Antidot Superlattices.* Graphene flakes used in these experiments were prepared by micromechanical exfoliation of natural graphite onto a degenerately doped p^{++} Si wafer with a thermally grown 90 nm SiO_2 dielectric. Layer metrology was subsequently performed using confocal μ-Raman spectrometry in order to identify mono-, bi-, and trilayer graphene flakes.[29,30] Following the initial characterization, various antidot superlattices were etched onto the flakes using electron beam lithography. Figure 1c shows two exemplary lattices with different filling fractions $F = \phi/s$ of antidots, where ϕ is the antidot diameter and s is their separation. In accordance with previous experimental results,[28,31,32] the corresponding Raman spectra display an

energetic shift and line width narrowing of the G band with increasing filling fraction, as shown in Figure 1a. The G band, which occurs at ~1580 cm^{-1} arises from doubly degenerate iTO and iLO phonon modes which possess E_{2g} symmetry. The observed stiffening (from 16.7 to 6.6 cm^{-1}) can be understood in terms of the Landau damping of the phonon mode, while the energetic shift arises from a renormalization of the phonon energy.[31−33] Furthermore, the energetic shift of the G band is positively correlated with the shift of the G′ band, as shown in Figure 1b, which is indicative of an effective p doping of the underlying graphene layer.[34,35] In contrast, a negative correlation in the energetic shifts of the G and G′ bands would imply n-doping.

In order to correlate shift and stiffening of the G band in antidot superlattices to an underlying carrier density, we fabricated electrically contacted devices without an antidot lattice, as shown schematically in Figure 2b. Using the electrical field effect of the back gate, the sheet carrier density Δn_s was modulated and the stiffening and energetic shift of the G band in the unpatterned samples was used to estimate the edge state density in the antidot superlattice (see Supporting Information). From these data the amount of p doping in the antidot samples was determined to reach up to 4×10^{12} cm^{-2} at a filling fraction of 2 (top axis in Figure.1a) and was not found to depend on the number of graphene layers as shown in Figure 1b. The large amount of effective p doping is rather remarkable since neither extrinsic dopants nor an external gate potential were applied to the antidot samples.

Furthermore, in order to investigate the microscopic origin of the observed p doping, we fabricated graphene−dye hybrids. Both, antidot flakes and electrically contacted devices were soaked in a 15 nmol solution of Rhodamine 6G (R6G), as shown schematically in Figure 2a. In these experiments, the R6G Raman peaks, the R6G fluorescence, and the Raman signal from graphene were monitored as a function of the antidot filling fraction F as well as different backgate and source−drain biases on the unpatterned flakes. In the subsequent discussion, we first focus on the R6G fluorescence signal.

Figure 3a shows a scanning electron micrograph of a single bilayer graphene flake with three distinct antidot superlattices L1, L2, and L3, which was used to study the spatially resolved μ-fluorescence of the R6G dye. The relative intensities of the broad fluorescence signal of the R6G molecule (recorded at $\lambda_{FL} = 577$ nm) normalized to the intensity of R6G fluorescence on the bare SiO_2 substrate are identified by circles in Figure 3a. Our results
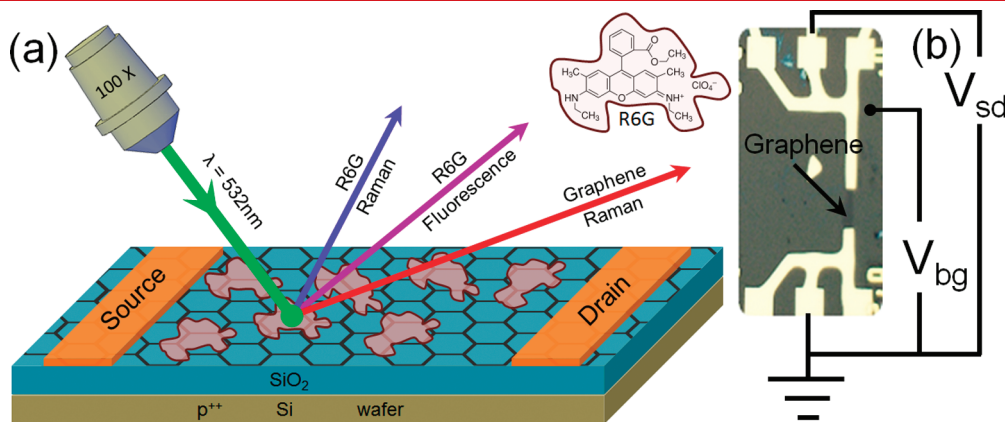

Figure 1. (a) The energetic shift (black diamonds) and broadening (blue triangles) of graphene's G band as a function of the antidot filling fraction. (b) Positive correlation of the energetic shifts of the G′ and G bands on different mono-, bi-, and tri layer samples, showing effective p doping. (c) Example scanning electron microscopy images of antidot lattices with different filling fraction.

Figure 2. (a) Schematic of the spatially resolved confocal μ-Raman experiment, showing the excitation beam ($\lambda_0 = 532$ nm) and the three optical signals, R6G SERS, R6G fluorescence, and graphene Raman, that were monitored during these experiments in both electrically gated and antidot devices. (b) An example of an electrically contacted graphene device used in these experiments.
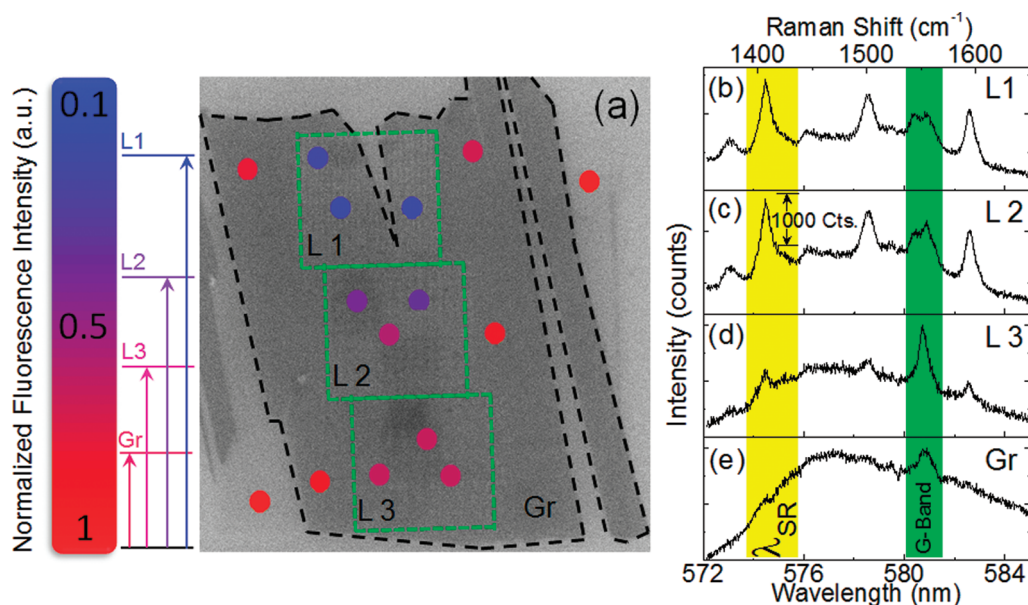
Figure 3. (a) Scanning electron micrograph of the graphene flake, with nanopatterned areas outlined by the green boxes. The filling fractions for lattice L1, L2, and L3 are 1, 1/2, and 1/3, respectively (all dots are 100 nm in diameter); the colors correspond to the R6G fluorescence in the sampling region normalized to the fluorescence on the bare SiO$_2$ wafer. Several example spectra taken on (b) lattice 1, (c) lattice 2, (d) lattice 3, and (e) unpatterned graphene, are also shown.

indicate that the R6G fluorescence is moderately quenched on the unpatterned graphene substrate as compared to the fluorescence on the bare SiO$_2$ wafer. Remarkably, the fluorescence becomes even stronger quenched in the region were the antidot superlattices are located. The amount of R6G fluorescence quenching increases with increasing filling fraction of the antidots as shown in panels b−e of Figure 3 for filling fractions of zero (graphene), 1/3 (L3), 1/2 (L2), and 1 (L1). The integrated intensity of the R6G fluorescence signal quenches up to a factor of 5 for the largest realized filling fraction, as shown in Figure 4.

In contrast to the quenching fluorescence signal, the intensity of the Raman signals from both R6G and graphene were found to increase 6-fold with increasing filling fraction, i.e., increasing density of edge states, as shown in Figure 4. In order to rule out any possible influence of the carboxylic bonds at the edges of the antidots and the possible presence of oxygen groups on SiO$_2$, which could have been introduced during oxygen plasma etching, a control experiment was performed in which several antidot lattices were reduced using 1 mmol of L-ascorbic acid for 24 h. Reduction in ascorbic acid was previously shown to effectively remove oxygen groups from graphene.[36,37] Our results (which are shown in the supporting online materials) indicate that no significant oxygen contamination occurs during the 10 s etching process and thus cannot be used to account for the observed enhancement of the Raman peaks.

Phenomenologically, the fluorescence quenching may be understood as follows. The incident laser light creates electron−hole pairs in the R6G dye. In the absence of the graphene substrate, the electron−hole pairs radiatively recombine thereby giving rise to the fluorescence signal on the bare SiO$_2$ wafer. It was previously shown that placing quantum dots on top of graphene results in an energy transfer from the dots into the underlying graphene layer,[38] resulting in a suppression of blinking from the quantum dots. A similar effect is expected to occur for the R6G molecules on graphene, where the radiative
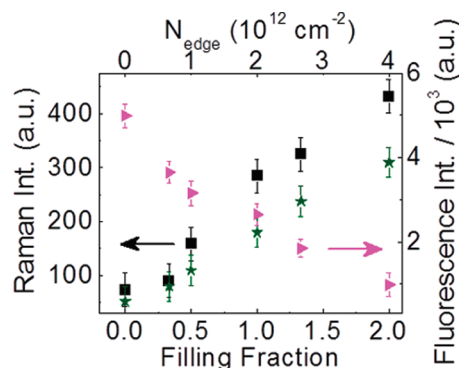

Figure 4. Integrated intensity of the fluorescence signal (pink triangles), right axis, and R6G Raman signals taken at 1390 cm^{-1} (black squares) and 1630 cm^{-1} (green stars), left axis, as a function of the antidot filling fraction.

recombination of the excitons in the R6G molecule is suppressed. In our experiments, additional quenching of the fluorescence signal in the antidot regions was observed (as shown in Figures 3 and 4). The additional quenching can thus be understood to arise from the extra states at the edges N_{edge}, which effectively prevent radiative recombination of the electron−hole pairs, and therefore quench the fluorescence signal. The amount of quenching observed in our experiments is rather remarkable since increasing the antidot filling fraction decreases graphene's surface area and introduces larger areas of SiO$_2$ into the excitation volume on which the fluorescence is not quenched.

The observed linear increase in carrier density with increasing filling fraction is in accordance with the theoretical prediction of Whimmer et al.,[21] who showed that the ratio of edge states to bulk states is given by

$$\frac{N_{edge}}{N_{bulk}} \approx 1.07(1 - 2\alpha)\frac{\hbar^2 v_F{}^2}{E_0{}^2 sR}$$
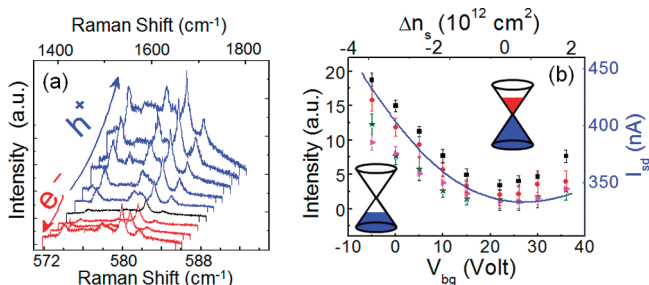
Figure 5. (a) Gate tunable R6G fluorescence of an unpatterned, electrically contacted device, similar to the one shown in Figure 2b, and (b) intensities of several Raman peaks (green stars taken at 1630 cm^{-1}and black squares taken at 1390 cm^{-1}), graphene's G band (red circles), and R6G fluorescence (pink triangles). The blue curve shows the source−drain current I_{sd}, which was used to determine the sheet carrier density Δn_s (top axis) measured in a separate transport experiment in the same sample prior to the addition of R6G.

where $\hbar$ is the reduced Planck's constant, v_F is the Fermi velocity in graphene, α is a parameter that characterizes edge roughness, E_0 is the energy width of the band of edge states, s is the antidot separation, and R is the antidot radius. Therefore, decreasing s or alternatively increasing R gives rise to a linear increase in N_{edge}.

Gate-Tunable Fluorescence. In order to further elucidate the mechanism for fluorescence quenching and the nature of N_{edge}, we fabricated electrically contacted and backgated graphene flakes, which did not contain an antidot superlattice. Varrying the backgate voltage, effectively moves the Fermi level in the device thereby affording the possibility of in situ electron and hole doping of the graphene flake according to

$$\Delta n_s = C_g(V_g - V_{Dirac})/e$$

where C_g is the gate capacitance, V_g is the applied gate voltage, V_{Dirac} is the location of the Dirac point, and e is the electron charge.[3,39−41] Modulating the Fermi level with the backgate creates a free sheet carrier density in the underlying graphene layer. The effect of free carriers on the R6G fluorescence and the R6G and graphene Raman is shown in Figure 5a, with the blue (red) traces corresponding to spectra from hole (electron) doped regions and the black trace was taken at the Dirac point. The intensities of several graphene and R6G Raman peaks are plotted in Figure 5b together with the $I_{sd}-V_{bg}$ trace (blue line), which illustrates that the current to the left of the minimum (the Dirac point) is due to hole conductivity, while the current to the right of the minimum corresponds to electron conductivity. As can be seen, the intensities of both the Raman peaks as well as the fluorescence signal can be either quenched or enhanced by the applied gate bias and directly follow the free carrier density in the device. Comparing the values of Δn_s (top axis in Figure 5b to N_{edge} (top axis in Figure 4) it is evident that the enhancement of the Raman peaks achieved in antidot devices occurs at comparable concentrations of N_{edge} and sheet carrier densities Δn_s in unpatterned samples, as shown in panels a and b of Figure 6. Unlike the Raman peaks, the R6G fluorescence is strongly quenched in the nanopatterned samples, whereas it is enhanced in the electrically gated samples. The contrasting behavior of the fluorescence signal is strongly indicative of the different nature of the carriers in the antidot superlattice as compared to unpatterned graphene and can be used to establish a microscopic mechanism for the observed fluorescence quenching and p-doping in the nanostructured samples.
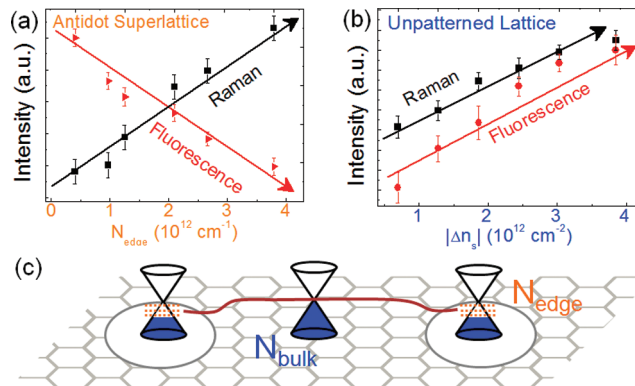
Figure 6. (a) Comparison of the fluorescence quenching in the nanopatterned samples as a function of edge state carrier density to (b) the enhancement of fluorescence in gated samples in which free carriers are injected into the conduction band. (c) A schematic of the band bending that occurs as a results of pinning the Fermi level at the localized density of states ρ_{edge} at the edges of the antidots (orange dashed lines).

In principle, two possible mechanisms could be responsible for fluorescence quenching: charge transfer from R6G into the trap states that are created by the additional edge state density or electrical field dissociation of the radiative R6G exciton, which leads to a strong decrease in the exciton recombination rate due to the reduced electron−hole wave function overlap in an electric field. Although charge transfer into trap states could account for the decrease of the fluorescence intensity, it cannot explain the observed stiffening and the energetic shift of the G-band phonon in graphene, both of which require an electric field effect.[31,32] In contrast, the field dissociation mechanism explains both phenomena, as well as the absence of fluorescence quenching in unpatterned graphene under backgate sweeping.

Since the edge states create spatially localized carriers, which are immobile, they would not cause the G-band stiffening. However, their presence effectively pins the Fermi level at the edges, thereby bending the band structure throughout the entire antidot superlattice, since no localized states exist in graphene's basal plane and the Fermi level must remain continuous, as shown schematically in Figure 6c. This band bending creates an effective potential, i.e., a built-in lateral electrical field, that accounts for the dissociation of the R6G excitons, resulting in the observed fluorescence quenching. In contrast, the vertical backgate field of the unpatterned graphene device does not lead to band bending, while the created free carrier density can effectively feed the carrier capture into the R6G molecules, causing the observed fluorescence enhancement. The Raman signals are enhanced by the electrical field mechanism providing free carriers in both cases.

Quantitatively, the effect of the built-in electrical field may be estimated to first order from the amount of p doping that it introduces. In graphene, doping is commensurate with the movement of the Fermi level into the conduction or valence bands by the electrical field. The band offset ΔE_F as a function of doping concentration n is given by $\Delta E_F = \hbar v_F k_F$, where $\hbar$ is the reduced Planck's constant, v_F is the Fermi velocity, and k_F is the Fermi wave vector, which in graphene is given by $k_F = (\pi n)^{1/2}$.[42] The antidot lattices used in our experiments yielded doping concentrations on the order of $(0.5-4.0) \times 10^{12}$ cm^{-2}, which correspond to band offsets of $\Delta E_F \approx 90-260$ meV.

The Fermi level pinning at the localized carrier density in the antidot superlattice is similar to Fermi level pinning of a Schottky barrier at an graphene—metal interface that is used to separate photogenerated carriers in optoelectronic devices based, for example, on carbon nanotubes.[9,16,18] In our case, however, no metal was deposited onto graphene and the pinning occurs at the localized edge states that are a direct consequence of the antidot superlattice.

In summary, we fabricated several graphene antidot super-lattices using mono-, bi-, and trilayer flakes and observed effective p-type doping which increases with larger filling fractions, as evident from their Raman signatures. We furthermore showed that after depositing R6G dye on these flakes, the corresponding fluorescence signal is strongly quenched with increasing antidot filling fraction, while the Raman signal is enhanced. These results are indicative to a microscopic mechanism in which the Fermi level becomes pinned at the antidot periphery giving rise to a built-in electric field, which accounts for the fluorescence quenching and the observed p-type doping in nanopatterned graphene. These findings make antidot lattices of great interest for carbon-based optoelectronics and might be particularly useful for light-harvesting applications such as photodetectors and solar cells requiring efficient field separation of electron—hole pairs.

■ ASSOCIATED CONTENT

ⓢ Supporting Information. Sample preparation and characterization, estimation of the effective p-doping concentration, and estimating the effect of possible oxygen contamination. This material is available free of charge via the Internet at http://pubs.acs.org.

■ AUTHOR INFORMATION

Corresponding Author
*E-mail: strauf@stevens.edu.

■ ACKNOWLEDGMENT

■ REFERENCES

(1) Novoselov, K. S.; Geim, A. K.; Morozov, S. V.; Jiang, D.; Zhang, Y.; Dubonos, S. V.; Grigorieva, I. V.; Firsov, A. A. *Science* **2004**, *306*, 666–669.

(2) Lin, Y. M.; Dimitrakopoulos, C.; Jenkins, K. A.; Farmer, D. B.; Chiu, H. Y.; Grill, A.; Avouris, P. *Science* **2010**, *327*, 662.

(3) Bolotin, K. I.; Sikes, K. J.; Jiang, Z.; Klima, M.; Fudenberg, G.; Hone, J.; Kim, P.; Stormer, H. L. *Solid State Commun.* **2008**, *146*, 351–355.

(4) Balandin, A. A.; Ghosh, S.; Bao, W.; Calizo, I.; Teweldebrhan, D.; Miao, F.; Lau, C. N. *Nano Lett.* **2008**, *8*, 902–907.

(5) Lee, C.; Wei, X.; Kysar, J. W.; Hone, J. *Science* **2008**, *321*, 385–388.

(6) Bonaccorso, F.; Sun, Z.; Hasan, T.; Ferrari, A. C. *Nat. Photonics* **2010**, *4*, 611.

(7) Novoselov, K. S.; Morozov, S. V.; Mohinddin, T. M. G.; Ponomarenko, L. A.; Elias, D. C.; Yang, R.; Barbolina, I. I.; Blake, P.; Booth, T. J.; Jiang, D.; Giesbers, J.; Hill, E. W.; Geim, A. K. *Phys. Status Solidi B* **2007**, *244*, 4106–4111.

(8) Neto, A. C.; Guinea, F.; Peres, N.; Novoselov, K.; Geim, A. *Rev. Mod. Phys* **2009**, *81*, 109–162.

(9) Xia, F.; Mueller, T.; ming Lin, Y.; Valdes-Garcia, A.; Avouris, P. *Nat. Nanotechnol.* **2009**, *4*, 839.

(10) Nair, R. R.; Blake, P.; Grigorenko, A. N.; Novoselov, K. S.; Booth, T. J.; Stauber, T.; Peres, N. M. R.; Geim, A. K. *Science* **2008**, *320*, 5881.

(11) Gierz, I.; Riedl, C.; Starke, U.; Ast, C. R.; Kern, K. *Nano Lett.* **2007**, *8*, 4603.

(12) Wang, Y.; Shao, Y.; Matson, D. W.; Li, J.; Lin, Y. *ACS Nano* **2010**, *4*, 1790.

(13) Wehling, T. O.; Novoselov, K. S.; Morozov, S. V.; Vdovin, E. E.; Katsnelson, M. I.; Geim, A. K.; Lichtenstein, A. I. *Nano Lett.* **2008**, *8*, 173.

(14) Dong, X.; Fu, D.; Fang, W.; Shi, Y.; Chen, P.; Li, L.-J. *Small* **2009**, *5*, 1422.

(15) Guo, B.; Liu, Q.; Chen, E.; Zhu, H.; Fang, L.; Gong, J. R. *Nano Lett.* **2010**, *10*, 4975–4980.

(16) Mueller, T.; Xia, F.; Freitag, M.; Tsang, J.; Avouris, P. *Phys. Rev. B* **2009**, *79*, No. 245430.

(17) Mueller, T.; Xia, F.; Avouris, P. *Nat. Photonics* **2010**, *4*, 297.

(18) Avouris, Ph. *Mater. Today* **2006**, *9*, 46–54.

(19) Hong, G.; Tabakman, S. M.; Welsher, K.; Wang, H.; Wang, X.; Dai, H. *J. Am. Chem. Soc.* **2010**, *132*, 15920–15923.

(20) Chen, Z.; Berciaud, S.; Nuckolls, C.; Heinz, T. F.; Brus, L. E. *ACS Nano* **2010**, *4*, 2964.

(21) Wimmer, M.; Akhmerov, A. R.; Guinea, F. *Phys. Rev. B* **2010**, *82*, No. 045409.

(22) Bai, J.; Zhong, X.; Jiang, S.; Huang, Y.; Duan, X. *Nat. Nano-technol.* **2010**, *5*, 190–194.

(23) Liang, X.; Jung, Y.-S.; Wu, S.; Ismach, A.; Olynick, D. L.; Cabrini, S.; Bokor, J. *Nano Lett.* **2010**, *10*, 2454–2460.

(24) Kim, M.; Safron, N. S.; Han, E.; Arnold, M. S.; Gopalan, P. *Nano Lett.* **2010**, *10*, 1125–1131.

(25) Sinitskii, A.; Tour, J. M. *J. Am. Chem. Soc.* **2010**, *132*, 14730–14732.

(26) Stojanovic, V. M.; Vukmirovic, N.; Bruder, C. *Phys. Rev. B* **2010**, *82*, No. 165410.

(27) Petersen, R.; Pedersen, T. G. *Phys. Rev. B* **2009**, *80*, No. 113404.

(28) Heydrich, S.; Hirmer, M.; Preis, C.; Korn, T.; Eroms, J.; Weiss, D.; Schuller, C. *Appl. Phys. Lett.* **2010**, *97*, No. 043113.

(29) Begliarbekov, M.; Sul, O.; Kalliakos, S.; Yang, E.-H.; Strauf, S. *Appl. Phys. Lett.* **2010**, *97*, No. 031908.

(30) Ferrari, A. C.; Meyer, J. C.; Scardaci, V.; Casiraghi, C.; Lazzeri, M.; Mauri, F.; Piscanec, S.; Jiang, D.; Novoselov, K. S.; Roth,, S.; Geim, A. K. *Phys. Rev. Lett.* **2006**, *97*, No. 187401.

(31) Yan, J.; Zhang, Y.; Kim, P.; Pinczuk, A. *Phys. Rev. Lett.* **2007**, *98*, No. 166802.

(32) Pisana, S.; Lazzeri, M.; Casiraghi, C.; Novoselov, K. S.; Geim, A. K.; Ferrari, A. C.; Mauri, F. *Nat. Mater.* **2007**, *6*, 198–201.

(33) Ferrari, A. C. *Solid State Commun.* **2007**, *143*, 47–57.

(34) Das, A.; Pisana, S.; Chakraborty, B.; Piscanec, S.; Saha, S. K.; Waghmare, U. V.; Novoselov, K. S.; Krishnamurthy, H. R.; Geim, A. K.; Ferrari, A. C.; Sood, A. K. *Nat. Nanotechnol.* **2008**, *3*, 210–215.

(35) Stampfer, C.; Molitor, F.; Graf, D.; Ensslin, K.; Jungen, A.; Hierold, C.; Wirtz, L. *Appl. Phys. Lett.* **2007**, *91*, 241907.

(36) Zhang, J.; Yang, H.; Shen, G.; Cheng, P.; Zhang, J.; Guo, S. *Chem. Commun.* **2010**, *46*, 1112–1114.

(37) Krauss, B.; Nemes-Incze, P.; Skalkova, V.; Biro, L. P.; von Klitzing, K.; Smet, J. H. *Nano Lett.* **2010**, *10*, 4544–4548.

(38) Chen, Z.; Berciaud, S.; Nuckolls, C.; Heinz, T. F.; Brus, L. E. *ACS Nano* **2010**, *4*, 2964.

(39) Stander, N.; Huard, B.; Goldhaber-Gordon, D. *Phys. Rev. Lett.* **2009**, *102*, No. 026807.

(40) Begliarbekov, M.; Sul, O.; Ai, N.; Yang, E.-H.; Strauf, S. *Appl. Phys. Lett.* **2010**, *97*, No. 122106.

(41) Tan, Y.-W.; Zhang, Y.; Bolotin, K.; Zhao, Y.; Adam, S.; Hwang, E. H.; Sarma, S. D.; Stormer, H. L.; Kim, P. *Phys. Rev. Lett.* **2007**, *99*, No. 246803.

(42) Hwang, E.; Adam, S.; Sarma, S. D. *Phys. Rev. Lett.* **2007**, *98*, No. 186806.